COMMUNICATION

Check for updates

Hydroxide ion-conducting viologen−bakelite organic frameworks for flexible solid-state zinc−air battery applications†

Deepak Rase, [iD] ‡[ab] Rajith Illathvalappil, [iD] ‡[ab] Himan Dev Singh, [iD] [ab] Pragalbh Shekhar, [iD] [ab] Liya S Leo,[ab] Debanjan Chakraborty, [iD] [a] Sattwick Haldar, [iD] [ab] Ankita Shelke,[c] Thalasseril G. Ajithkumar[c] and Ramanathan Vaidhyanathan [iD] ⋆[ab]

Adaptable polymer-based solid-state electrolytes can be a game-changer toward safe, lightweight flexible batteries. We present a robust Bakelite-type organic polymer covalently decked with viologen, triazine, and phenolic moieties. Its flexible structure with cationic viologen centers incorporates counter-balancing free hydroxide ions into the polymeric framework. By design, the aromatic groups and heteroatoms in the framework can be activated under an applied potential to prompt a push−pull drive, setting off the towing of hydroxide ions *via* weak electrostatic, van der Waals, and hydrogen-bond interactions. The frontier orbitals from a DFT-modeled structure certify this. The hydroxyl-polymer requires minimal KOH wetting to maintain a humid environment for Grotthuss-type transport. The hydroxide ion conductivity reaches a value of 1.4×10^{-2} S cm^{-1} at 80 °C and 95% RH, which is retained for over 15 h. We enhanced its practical utility by coating it as a thin solid-state separator-cum-electrolyte on readily available filter paper. The composite exhibits a conductivity of 4.5×10^{-3} S cm^{-1} at 80 °C and 95% RH. A zinc−air battery (ZAB) constructed using this polymer-coated paper as electrolyte yields a maximum power density of 115 mW cm^{-2} and high specific capacitance of 435 mA h g^{-1}. The power density recorded for our ZAB is among the best reported for polymer electrolyte−based batteries. Subsequently, the flexible battery fabricated with IISERP-POF11_OH@FilterPaper exhibits an OCV of 1.44 V, and three batteries in series power a demo traffic signal. To underscore the efficiency of hydroxide ion transport through the complex multifunctional backbone of the polymer, we calculated the diffusion coefficient for OH$^-$ (Exp: 2.9×10^{-5} cm^2 s^{-1}; Comp. 5.2×10^{-6} cm^2 s^{-1}) using electrochemical methods and MD simulations. Climbing-edge NEB calculations reveal a large energy barrier of 2.11 eV for Zn^{2+} to penetrate the polymer and identify hydroxide ions within the polymer, suggesting no undesirable Zn^{2+}

New concepts

In metal–air batteries, hydroxide ions produced at the cathode *via* the reduction of oxygen from the air need to be efficiently transported to combine with metal ions generated by anodic oxidation. A liquid electrolyte such as KOH$_{(aq)}$ typically transports ions. This transport of ions suffers from evaporation of the solvent over time; KOH is gellified to minimize this. However, in the gel, the electrostatic interaction between K$^+$ and OH$^-$ restricts facile movement of the latter ion. A passivating layer of K$_2$CO$_3$ also forms on the anode surface, creating internal resistance. To overcome this, we developed a cationic polymer with counter-balancing OH$^-$ ions in their nanopores. The advantages are many. For example, the polymer is a steady source of OH$^-$ ions since they are in a stoichiometric ratio with the cationic sites. There is no major solvent dependence, so there are fewer problems with electrolyte evaporation. Minimal use of KOH avoids K$_2$CO$_3$ formation. Our insoluble polymer is a safe and humidity-withstanding solid-state electrolyte. This cationic polymer transports OH$^-$ ions effortlessly and prevents undesirable crossover of Zn^{2+} ions, yielding high power density. Furthermore, this bulk cationic framework does not compete with hydroxide-ion diffusion during operation, which lowers internal resistance.

crossover. Our findings assert the readily accessible C−C-linked cationic polymer's capacity as a solid-state electrolyte for ZABs and any anion-conducting membrane.

Introduction

Hydroxide ion-conducting materials are receiving substantial attention owing to their significance in green technologies such as anion exchange membrane fuel cells (AEMFCs), metal–air batteries and water electrolyzers.[1–3] Typically, hydroxide ions

[a] Department of Chemistry, Indian Institute of Science Education and Research, Dr Homi Bhabha Road, Pashan, Pune 411008, India. E-mail: vaidhya@iiserpune.ac.in, vaidhya@acads.iiserpune.ac.in

[b] Centre for Energy Science, Indian Institute of Science Education and Research, Dr Homi Bhabha Road, Pashan, Pune 411008, India

[c] Central NMR Facility and Physical/Materials Chemistry Division, CSIR-National Chemical Laboratory, Dr Homi Bhabha Road, Pune 411008, India

† Electronic supplementary information (ESI) available. See DOI: https://doi.org/10.1039/d2nh00455k

‡ D. R and R. I contributed equally to this work.

exhibit low conductivity compared to protons owing to their sluggish diffusion and higher mass.[4] Proton-conducting materials are also well established and commercialized for various energy applications.[5–7] In comparison, hydroxide ion-conducting materials are still in their infancy. Hence, the rational design of hydroxide ion-conducting materials is beneficial and would pave the way for application-specific charge-storage devices.

The rapid increase in energy demand has drawn ample attention to charge storage devices.[8,9] To manage the ever-increasing energy demand, it is necessary to develop efficient and cost-effective charge storage devices.[10,11] In this regard, zinc–air batteries (ZABs) are receiving wide attention owing to their high energy density, low cost and safety. Furthermore, they have been used for many applications such as hearing-aid devices, cameras, and grid-scale energy storage.[12–15] The development of high-performing ZABs requires the advancement of electrodes and separators.[16,17] Besides the electrode kinetics, hydroxide ion transport through the electrolyte largely determines the efficiency of ZABs.[18] Liquid-based electrolytes create complications in fabricating or handling the devices, and achieving a long cycle life.[19,20] In comparison, the solid-state electrolytes are less problematic in this regard. Furthermore, their leakage-proof framework offers superior safety features.[21] Therefore, developing ZABs with solid-state separators that concomitantly possess improved performance and flexibility would benefit applications.[22] However, the key bottleneck associated with the hydroxide ion-conducting materials is their low ionic conductivity and poor stability under harsh chemical environments.[23] Several ion-conducting (H^+ or OH^-) materials with better conductivity have been reported in the literature in the pelletized state, but their practical potential as a thin and free-standing solid-state separator has not been explored.[4,24–27] Hence, we developed a thin hydroxide ion-conducting solid-state separator-cum-electrolyte for ZAB from the cationic polymer by coating it on filter paper (FP), adopting a simple dip-coating strategy.

Various kinds of separators have been employed for ZABs to transport OH^- ions, and some porous separators provide satisfactory battery performance.[14,28] A fundamental issue associated with the porous separators is the passage of zincate ions $(Zn(OH)_4^{2-})$ through the pores.[29] For example, the Celgard separators have good chemical stability and low cost. However, the significant transport of zincate ions from the anode to the cathode through the porous separator does occur, resulting in performance loss during the ZAB operation. One can overcome this by integrating the porous separators with the hydroxide ion-conducting insoluble materials. This would block the pores, allowing the passage of OH^- ions, and restrict the movement of zincate ions.[30] Polymers have been intensely probed for their stability advantage.[31] Recently, amide polymers constructed from simple monomers (acyl chloride + melamine) were shown to possess strengths comparable to steel.[32] This inspired us to explore the potential of simple systems such as Bakelite and viologen for this task-specific application. Towards this approach, we have synthesized triazine-resorcinol and viologen-based

cationic polymeric organic frameworks (POFs) with enriched hydroxyl (–OH) groups.[33] These POFs can be obtained in a large scale *via* a one-pot synthesis using Bakelite chemistry: forming robust C–C bonds without any catalyst.[34] Such types of POFs are chemically robust, thermally stable and have found use in a wide range of applications, including energy storage, gas storage, catalysis, and anion exchange.[35–38] The viologen-based quaternary center is counterbalanced by the larger anion like Br^-, which finds easy exchange with OH^- ions. Recently, our group reported a family of cationic POFs, among which IISERP-POF11 (**1**) demonstrated excellent performance for the anion exchange.[38] Therefore, in the present work, the hydroxide ion-exchanged IISERP-POF11, IISERP-POF11_OH (**1_OH**), was integrated with cellulose paper (IISERP-POF11_OH@Filter Paper, **1_OH@FP**) and employed as the solid-state separator-cum-electrolyte for zinc–air battery applications. The integrated system displayed an improved performance for the ZAB, and validated the suitability of employing **1_OH** for energy applications.

Results and discussion

Synthesis and bulk characterizations of as-made IISERP-POF11 (1) and hydroxide exchanged IISERP-POF11_OH (1_OH)

The synthesis of **1** from the monomers and its further conversion into **1_OH** after the exchange of the Br^- with OH^- ions is illustrated in Scheme 1 (the detailed synthesis procedure is provided in the ESI†). The formation of the as-synthesized polymer was confirmed by various characterization techniques, such as NMR, FTIR, FESEM, HRTEM, TGA, and N_2 adsorption isotherm measurements. ^{13}C cross-polarization (CP) magic angle spinning (MAS) solid-state nuclear magnetic resonance (NMR) studies indicated the presence of Bakelite type coupling between triazine-resorcinol and viologen-based bipyridinium aldehyde (Fig. 1a). Furthermore, some unsubstituted sites on the phloroglucinol rings led to the formation of a characteristic aliphatic C–C bond, which was observed around 26 ppm (Fig. 1a).[39–41] It was followed by the other characteristic peaks from aromatic groups like triazine around 172 ppm (i) and aromatic peak around 151 ppm (h). The aliphatic peaks for the building blocks around 65 ppm (b) were intact. This demonstrates that the polymerization is taking place. However, to confirm the stability of the polymer powder, we recorded the IR and NMR spectra of the material subjected to boiling in a THF + DMF mixture, followed by a 24 h soak in 6 M KOH solution. All of the characteristic peaks remained intact, and were positioned at similar chemical shifts with matching intensity. This exceptional chemical stability and the functional group integrity of the polymer, especially towards harsh treatments, is highly desirable for electrolyte applications (Fig. S1, ESI†). Subsequent to the anion exchange (Br^- with OH^- ions), a significant color change from brown to yellow was observed, and is represented with the photographic images in Scheme 1.

Fig. 1b shows the comparative IR spectra of the monomers, *i.e.*, 1,1′-bis(4-formylbenzyl)-4,4′-bipyridiniumdibromide (VBrBA), 4,4′,4″-(1,3,5-triazine-2,4,6-triyl)tris(benzene-1,3-diol) (TRIRES),
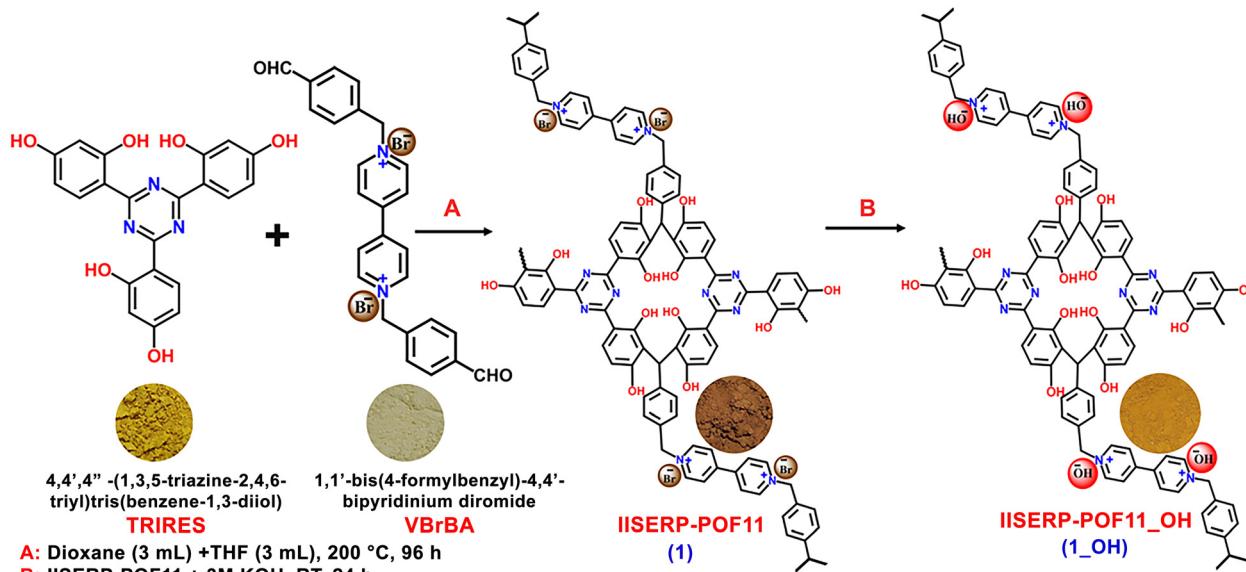
Scheme 1 Synthetic procedure of **1_OH**. Insets present photographs of the corresponding compounds.

the as-synthesized cationic polymer (**1**), and its hydroxide exchanged form, **1_OH**. The disappearance of the C=O (1690 cm^{-1}) feature from the monomer VBrBA with the polymerization confirms the C–C bond formation between the aldehyde and the phenolic moieties (Scheme 1). Furthermore, the presence of C=N (1620 cm^{-1}) assures that the building blocks are intact in **1** and **1_OH** (Fig. 1b). The field emission scanning electron microscopy (FESEM) images of **1** indicate that the particles are either connected or intergrown microspheres of different diameters ranging from 500 nm to 2 μm (Fig. 1c and Fig. S2, ESI†). Fig. 1d and Fig. S3 (ESI†) confirm that there is no deformation in the shape of these microspheres after treating with 3 M KOH solution, *i.e.*, on the formation of **1_OH**. This indicates their textural stability under the harsh corrosive environment. Thus, **1_OH** could be suited for operating under concentrated alkaline conditions. In the energy dispersive X-ray (EDX) analysis, the drop in the atomic percentage of Br^{-} ions from 1.74% to 0.21% confirms the effective exchange of Br^{-} ions with OH^{-} to form **1_OH** (Fig. S4 and S5, ESI†). The K^{+} ion traces in **1_OH** is negligible, which confirms that the hydroxide ions are counterbalanced by the cationic centers of the polymer. The high-resolution transmission electron microscopy (HRTEM) images of **1** and **1_OH** are displayed in Fig. 1e and f, respectively. The HRTEM showed that the spherical balls in **1_OH** are continuously connected, which could aid the ionic transport across grains and spheres. After OH^{-} ion exchange, we noticed a slight decrease in the surface diameter of **1_OH** spheres. This could be due to more compacting from OH^{-} compared to Br^{-}. However, the spherical morphology is still intact (Fig. S6 and S7, ESI†).

Thermogravimetric analysis in Fig. 1g revealed that the framework **1** is stable at temperatures up to 280 °C. We attribute this to the strong C–C bond formed between the monomers, resembling Bakelite. The cationic polymer treated with 3 M (**1_OH**) and 6 M KOH (**1_6OH**) display slightly different TGA profiles (Fig. 1g and Fig. S8a, ESI†), but their

thermal stabilities are comparable. The contact angle measurements pointed at the surface of the as-made polymer powder, **1** being super-hydrophobic. However, the **1_OH** prepared by anion exchange in an aqueous alkaline solution yielded a final powder that was hydrophilic (Fig. 1h and Fig. S8b, S8c, ESI†). This surface wettability is crucial for the material's interaction with electrolytes. We investigated the intrinsic porosity with water sorption isotherms. The water adsorption isotherms of **1** and **1_OH** showed a very similar profile, indicating that there were no major changes to the pore environment or structure. The overall water capacity of **1_OH** is higher than that of **1**, suggesting improved intrinsic wettability. Thus, the near super-hydrophobic (148° ± 3°) material with Br^{-} containing framework becomes much more hydrophilic when exchanged with OH^{-}. Notably, there was no noticeable swelling of the polymer or significant change in density.

The density functional theory-based model fitted to the 77 K N$_2$ isotherm shows the majority of the pores being 15 to 18 Å in size, which are still intact after the ion exchange (Fig. S9, ESI†). However, the N$_2$ uptakes are nominal, which is expected as the pores are permanently occupied by the counter-balancing anions. Still, there is sufficient openness to support the transport of OH^{-} ions. Furthermore, unlike the crystalline frameworks, these polymers exhibit structural flexibility with changing humidity, opening up spaces for dynamic interactions between the framework atoms and the free hydroxide ions. This impacts the electrolyte's wetting and hydroxide ion transport characteristics (Fig. 1h).

Electrochemical studies

Electrochemical impedance analysis was performed in the frequency range of 10^6 to 0.1 Hz with an AC amplitude of 10 mV using a Solartron impedance analyzer. The impedance was recorded at variable temperatures from 30 °C to 80 °C with a constant relative humidity of 95%, and the data are presented
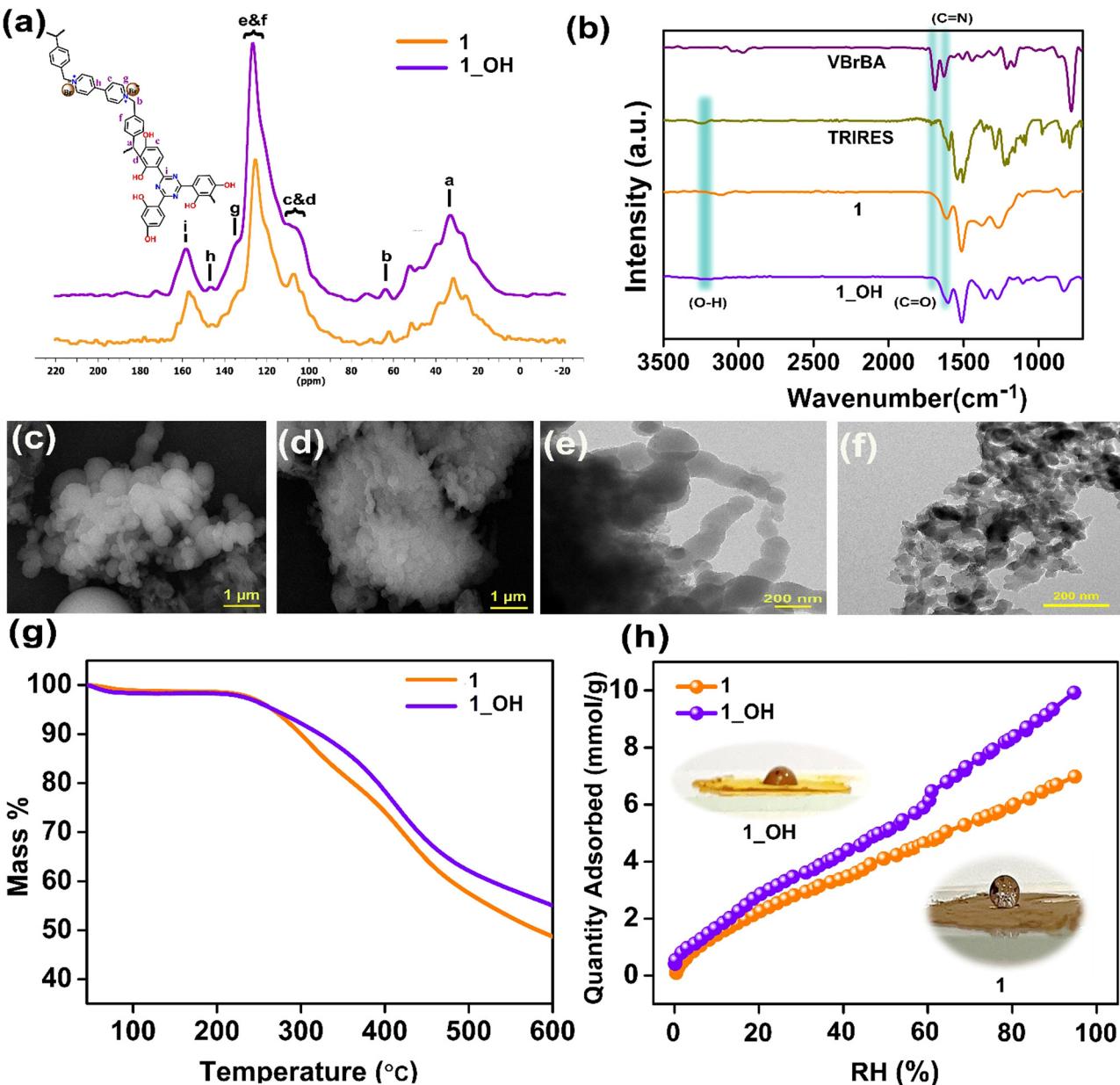
Fig. 1 (a) ^{13}C-CPMAS spectra of **1** and **1_OH**; (b) IR spectra of TRIRES, VBrBA, **1**, and **1_OH**; (c and d) FESEM images of **1** and **1_OH**; (e and f) HRTEM images of **1** and **1_OH**; (g) thermogravimetric analysis of **1** and **1_OH** under N$_2$ atmosphere at a ramp rate of 5 °C min^{-1}; and (h) water adsorption isotherms of **1** and **1_OH** with insets presenting photographs from the contact angle measurements.

in Fig. 2a. To evaluate the intrinsic conductivity of **1_OH**, the measurements were performed on a densely pressed pellet of the same. The equivalent circuit was employed for fitting all of the Nyquist curves, using the Zview-4 software. At a constant relative humidity of 95%, the OH$^-$ ion conductivity value increased from 2.7×10^{-4} S cm^{-1} at 30 °C to 1.4×10^{-2} S cm^{-1} at 80 °C (Fig. 2a and Table S1, ESI†). In order to check the humidity-dependent conductivity of **1_OH**, we measured the ac-impedance at 80 °C by varying the humidity (60% RH, 80% RH and 95% RH) (Fig. S10a, ESI†). The conductivity values are 3.6×10^{-5}, 3.8×10^{-4} and 1.4×10^{-2} S cm^{-1} at RH values of 60%, 80% and 95%, respectively. The increase in hydroxide ion conductivity at 80 °C with increasing temperature suggests lowering of the activation

energy, while the increase in conductivity with increasing humidity suggests that water could be playing a crucial role *via* hydrogen bonding.[42] Fitting an Arrhenius equation to this temperature-dependent impedance data yields an activation energy of 0.52 eV (Fig. 2b), suggesting a mixed Grotthuss–Vehicular diffusion mechanism.[43] The observed activation energy is comparable to some of those reported for hydroxide ions in other nanoporous structures.[44] An equivalent circuit fit to the most promising Nyquist plots (80 °C, 95% RH) reveals an Ohmic resistance of 3.2 Ω (neat pellet) (Fig. 2c). In the fitted equivalent circuit, we confirmed the need for a CPE component, by measuring the CV of **1_OH**, which clearly indicated the presence of capacitive behavior (Fig. S11, ESI†). In our case,
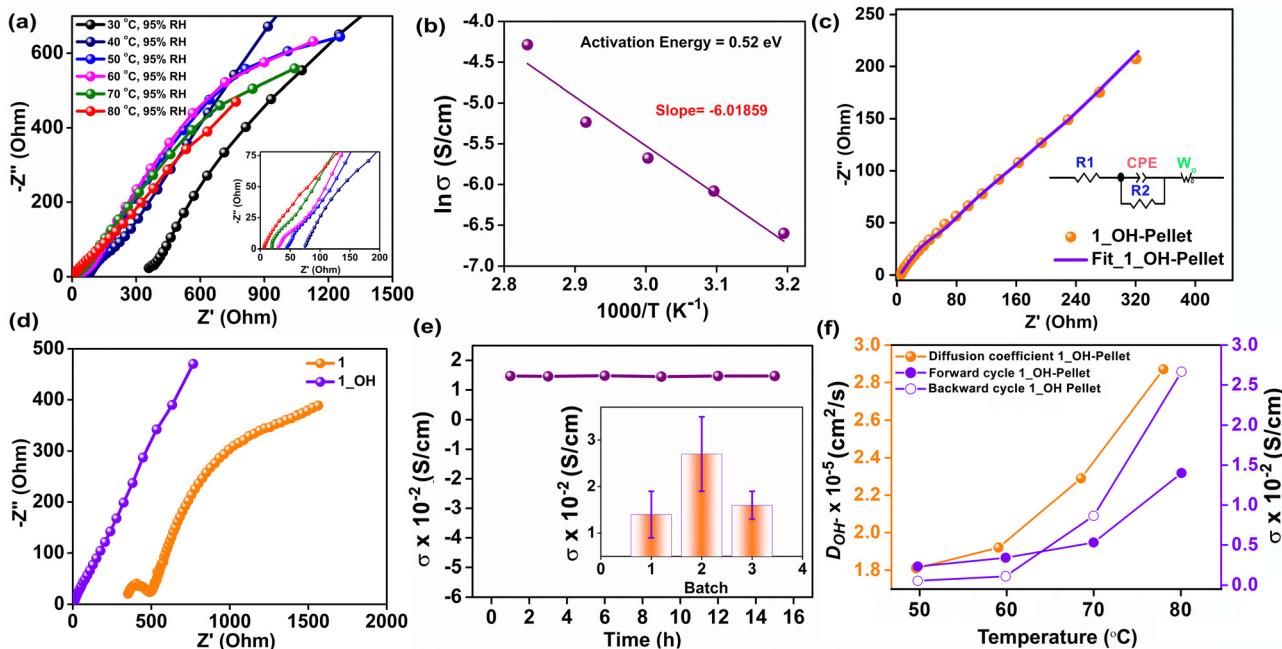
Fig. 2 (a) Nyquist plots from the temperature-dependent conductivity measurements of **1_OH**; inset presents its zoomed-in view. (b) Arrhenius plot of **1_OH**. (c) Equivalent circuit fit to the Nyquist plot of **1_OH** at 80 °C and 95% RH. (d) Comparison of the Nyquist plots of **1** containing Br⁻ as the counter ion *vs.* **1_OH**. (e) Conductivity of **1_OH** at 80 °C and 95% RH recorded for 15 h; inset shows that the conductivity is reproducible across different batches of the sample. (f) Hydroxide ion diffusion coefficient and forward–backward cycling plot for the OH⁻ conductivity of **1_OH** at different temperatures and constant relative humidity of 95%.

considering that the hydroxide ion is moving in channels lined with hydroxyl groups and triazine, both of which might provide some hydrogen bond assistance resulting in the Grotthuss mechanism. Simultaneously, under the applied ac-potential, there could also be sufficient force for vehicular motion. Due to the absence of OH⁻ ions in the pristine polymer (**1**), it shows a poor ionic conductivity value of 7.39×10^{-5} S cm⁻¹ at 80 °C and 95% RH. This is expected as the Br⁻ ions are heavier and will be even less effective for a hydrogen-bond-assisted Grotthuss-type movement. Furthermore, the comparison of the equivalent circuit fitted Nyquist plots of **1** *vs.* **1_OH** (Fig. 2d) suggests that the series resistance and charge-transfer resistance are both substantially higher for **1** (R1 = 352 Ω, R2 = 509 Ω) compared to the **1_OH** (R1 = 3.2 Ω, R2 = 11.8 Ω). The large semicircle in the low-frequency regime in the case of **1** suggests limited or restricted diffusion even in the same time-scale of measurements as employed for the **1_OH**. Meanwhile, **1_OH** has a typical semi-infinite linear diffusion; that is, diffusion in one dimension, which is only bound by a large planar electrode on one side (45° angle with *Z*'-axis), a typical Warburg behavior. A CPE-P value close to 0.5 for the **1_OH** pellet is suggestive of pseudo-capacitive behavior, which is expected for the polymer with porous structure (Fig. 2c). Remark: A transmission line model mimicking the Fickian diffusion, wherein the movement of ions through the pores is coupled to the movement of electrons through the pore walls, was not chosen. This is considering that the polymer does not have a crystalline structure with highly ordered pores, and also the electronic conductivity in larger length scales is limited.[45] Linear sweep voltammetry (LSV) was

conducted to check the electronic conductivity of **1_OH** in the potential window of −0.6 to 0.6 V with a scan rate of 10 mV s⁻¹ (Fig. S12, ESI†). **1_OH** shows negligible electronic conductivity, which suggests that the observed conductivity is predominantly ionic, arising from the OH⁻ ions. To assess the ability of **1_OH** in delivering a stable hydroxide-ion conductivity, we measured it at 80 °C and 95% RH for 15 h. There is a build-up of a small charge transfer resistance over 15 h. Furthermore, **1_OH** retains >95% of its conductivity (Fig. 2e and Fig. S10b, ESI†). This hydroxide ion conductivity is reproducible across different batches of the sample (Fig. 2e inset). To check the cyclic stability of **1_OH** for OH⁻ transport, the pellet was dried overnight at 100 °C in a vacuum oven. Impedance analysis was then carried out for both the forward cycle (increasing the temperature from 30 to 80 °C at 95% RH) and the backward cycle (decreasing the temperature from 80 to 30 °C at 95% RH) (Fig. 2f). The conductivities remained the same during the cycling, reflecting the electrochemical stability of the polymer. Furthermore, the shape/profile of the Nyquist plots remained the same, suggesting that the pathway and the mechanism of conduction remained unchanged. We calculated the diffusion coefficient for the hydroxide ions inside the cationic polymer framework using the Z' *vs.* $\omega^{-1/2}$ plot. The low-frequency spectrum of the impedance plot yielded the characteristic linear fits (Fig. S13, ESI†), from which the diffusion coefficients were estimated to be 2.9×10^{-5} cm² s⁻¹ at 80 °C with 95% RH. The diffusion coefficient increased systematically with an increase in temperature (Fig. 2f). The calculated diffusion coefficients matched well with the theoretical values reported in the literature.[46,47] However, we could not find any experimentally

calculated diffusion coefficients for hydroxide ions inside a porous material. However, for Cl⁻, the diffusion coefficient is on the order of 10^{-8} cm² s⁻¹.[48]

Conductivity characteristics of 1_OH coated on Filter Paper (1_OH@FP)

Encouraged by the appreciable hydroxide ion conductivity and stability exhibited by this viologen polymer, we set out to investigate its scope as a solid-state electrolyte in a zinc–air battery. It is hugely advantageous to coat the polymer on a porous filter paper, which provides a bulk wettable microporous-macroporous separator-cum-electrolyte membrane. However, the composite needs to retain the high levels of OH⁻ ion conductivity. To investigate this, **1_OH** was devised into a separator-cum-electrolyte by coating it onto a research-grade Whatman filter paper (**1_OH@FP**). The commonly available filter paper was chosen owing to its advantageous features, such as low cost, lightweight, flexibility and easy accessibility.[49] The dip-coating method was used to deposit the polymer by soaking cellulose paper in a dispersed solution of **1_OH** in water. The process is scalable and 25 cm² **1_OH@FP** was prepared in a few hours. The fluorescence microscopy images illustrated in Fig. 3a show the loss of fluorescence of the **FP** upon loading with the polymer. Its uniform loading on paper is evident. Typically, the filter paper has entangled cellulose fibers (Fig. 3b). These fibers are rich in terminally placed binding groups, which are likely to be compatible with our hydroxyl-functionalized polymer backbone. The solid-state UV-Vis absorption spectra of neat **FP** vs. **1_OH@FP** showed lowering of the absorbance

intensity (@280 nm) of the FP upon coating with the polymer (Fig. S14, ESI†). This is in agreement with the results from the fluorescence microscopy. These suggest that the polymer directly contacts the electrolyte and the electrodes, while the paper is acting as a separator. From the FESEM images, it is evident that the polymer composite is deeply buried within the cellulose matrix of the paper (Fig. 3b, c and Fig. S15, S16, ESI†). This could be crucial to providing an intimate contact between the two entities in the composite. The cross-sectional SEM analysis of **1_OH@FP** indicated that the distribution of **1_OH** is uniform in FP. The fibers of the FP are intimately blended to a good thickness (not merely coating the surface) with small granules of **1_OH**. (Fig. S16, ESI†). Even a strong thumb-pressure does not make the polymer particles lose its adhesion with the paper. The hydroxide ion conductivity of **1_OH@FP** was analyzed at 80 °C and 95% RH, and the Nyquist plot is presented as Fig. 3d and Fig. S17 (ESI†). **1_OH@FP** shows a OH⁻ conductivity value of 4.5×10^{-3} S cm⁻¹ at 80 °C and 95% RH (R1 = 10.4 and R2 = 18.2 Ω), which is quite comparable to the values obtained with the pellets at similar operating conditions. The same equivalent circuit fits extremely well. From the fitted data, we observe that the resistances of the **1_OH@FP** is relatively higher. This is expected as more interfaces are generated and the paper is much less conductive. Notably, the CPE value of **1_OH** (0.45) increases to 0.72 for **1_OH@FP**, indicating the increase in double layer capacitive character. Interestingly, the ion diffusion is noticeably improved when the material is coated on the FP (Fig. S18 ESI†). Comparing the Warburg tail of the **1_OH** pellet vs. the **1-OH@FP** brings some
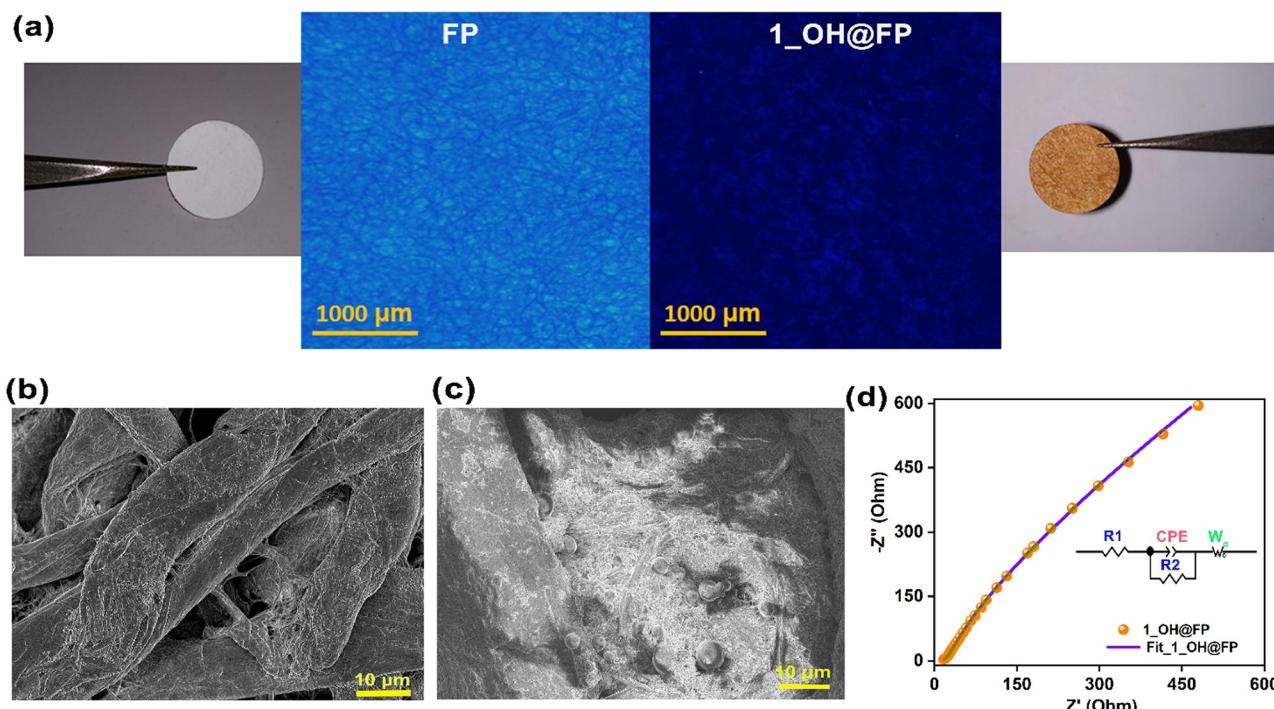

Fig. 3 (a) Macro zoom fluorescence microscope images of neat FP and **1_OH@FP** with the corresponding photographs on the side. (b, c) FESEM image of neat FP and **1_OH@FP**. (d) Equivalent circuit fit to the Nyquist plot of **1_OH@FP** at 80 °C and 95% RH.

noteworthy features. At lower frequencies, the diffusion tail of **1_OH@FP** starts to deviate more from making an angle of 45° with the *x*-axis. This indicates deeper penetration of the ions into the material even at these low frequencies. This is expected, as the active material is coated on a paper to form a much thinner electrolyte membrane compared to the pellet. This points at the advantage of making this paper-derived electrolyte-cum-separator unit. Importantly, the overall conductivity still remains very much in an acceptable regime for a hydroxide-ion conducting electrolyte. Thus, the **1_OH@FP** provides an appropriate electrolyte material with a micro-macroporous structure that still inhibits the direct zincate ion crossover through the separator. These properties are crucial for the battery performance.

1_OH@FP as solid-state electrolyte in ZAB

The excellent ionic conductivity of **1_OH@FP** motivated us to use it for zinc–air battery applications. For this, **1_OH@FP** was employed as the solid-state separator-cum-electrolyte by sandwiching between the electrodes. Fig. 4a depicts the schematic of the zinc–air battery assembly with its components (Fig. S19, ESI†). During discharge, oxygen electrocatalytically reduces to form hydroxide ions at the cathode.[50] At the anode, zinc would oxidize to Zn^{2+}. The zinc ions would react with the hydroxide ions coming from the cathode through the separator to form zincate ions and further to ZnO. To assess the performance of **1_OH@FP** in ZAB, LSV was performed at a scan rate of 10 mV s^{-1}, and is shown in Fig. 4b. The polarization analysis presented in Fig. 4b shows a maximum power density of 115 mW cm^{-2} for the **1_OH@FP** based battery compared to 38 mW cm^{-2} obtained for the neat filter paper-based counterpart. The resistances of

the **1_OH@FP** *vs.* neat **FP** were determined from impedance analysis performed on their respective ZAB assemblies. The Ohmic drop in **1_OH@FP** is notably lower compared with neat **FP** (1.55 *vs.* 2.1 Ω) (Fig. S20 and S21, ESI†). Furthermore, the resistance increases almost by 0.85 Ω during the use of the neat **FP** as the electrolyte support in the battery, which was run for about 2 h. In contrast, the **1_OH@FP**, maintains almost the same resistance even after 8 h under a comparable battery setup. It is worth mentioning that even a difference of 0.55 Ω (between **FP** *vs.* **1_OH@FP**) hugely impacts the power density (Fig. 4b), as well as the run time of the ZAB derived out of these electrolyte supports. Accordingly, the **1_OH@FP** containing battery exhibits a higher specific capacitance of 435 mA h g^{-1} compared to 397 mA h g^{-1} obtained for the neat **FP** based battery. Furthermore, the Fig. 4c inset shows that the **1_OH@FP** containing battery delivers four times more run time compared with **FP** based ZAB. Flexible solid-state ZAB was fabricated to show the practical applicability of the as-prepared **1_OH@FP** (details provided in the experimental section). The fabricated solid-state battery offers an OCV value of 1.44 V in an air atmosphere (without purging any additional O$_2$ gas). Three flexible devices connected in series yielded an output of 4.22 V (Fig. S22, ESI†). The output voltage was stable to bending and twisting (Fig. 4d) owing to the liquid-free nature of **1_OH@FP**. By combining the batteries in series, we could power three light-emitting diodes (LEDs) connected in parallel, resembling the traffic signal lights (Fig. 4e). Furthermore, 10 months after fabrication, we were able to regenerate the OCV of 1.10 V on wetting the device with just 50 μL of water (Fig. 4f). Overall, the results indicate the feasibility of employing **1_OH@FP** as the hydroxide ion-conducting material for flexible batteries.
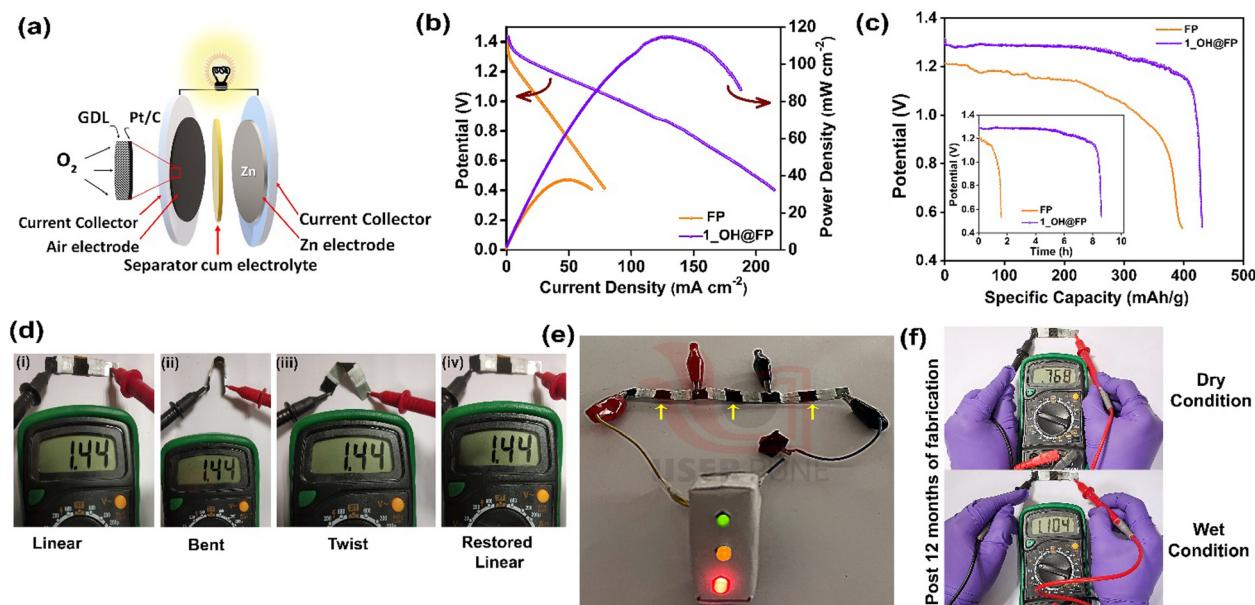

Fig. 4 (a) Schematic of the ZAB with its components. (b) Polarization plot of neat FP and **1_OH@FP**-based ZAB. (c) Comparative specific capacity of neat FP and **1_OH@FP** based batteries; inset shows the durability of the ZAB over time. (d) Photographs showing constant OCV at different flexible modes of the solid-state ZAB. (e) Image of the flexible solid-state ZAB powering a demo traffic signal with yellow arrows indicating the air-breathing cathode. (f) OCV regeneration of solid-state ZAB after 10 months of fabrication on wetting with water.

Post ZAB usage stability analysis of 1_OH@FP

The stability of **1_OH@FP** when employed as separator-cum-electrolyte in the ZAB was investigated. PXRD and IR analysis indicated that the polymer remained intact on the FP even after the complete discharge cycle (8 h) (Fig. S23 and S24, ESI†). Then, this composite electrolyte in the ZAB, **1_OH@FP**, was subjected to high-frequency impedance analysis after a complete discharge cycle and compared with the neat FP's performance (Fig. S20 and S21, ESI†). The resistance remains the same for the **1_OH@FP**, but increases for the neat FP. This is due to the relatively higher loss of KOH (aqueous solution) from the neat FP, creating a passivation layer that is unfavorable for the conduction. This problem is not observed in the case of **1_OH@FP**. This is most likely due to the intrinsic tendency of the polymer to hold onto the OH⁻ species driven by its charge-balance requirements, and their pores trap water more efficiently (Fig. 1h). Furthermore, in the case of **1_OH@FP**, the conduction pathway and diffusion mechanism remain the same, as seen from the equivalent circuit fits. The post-ZAB microscopy analysis of the **1_OH@FP** further confirms the homogeneous adherence of the active material on the FP (Fig. S25 and S26, ESI†).

Push–pull electronics in the triazine-resorcinol-viologen framework portrayed by frontier orbitals

To investigate the potential role of the cationic polymers in interacting with the hydroxide ion movement in this viologen functionalized spongy polymer, we looked at the potential/electron distribution within the polymer backbone. As a coherent step, we replaced the heteroatoms within the covalently linked modules and monitored the impact it brings to the HOMO–LUMO distribution. The local electronics is likely to be dictating the hydroxide-framework (heteroatom) interactions. For this, we developed a two-repeat unit polymer using the Random Copolymer module in the Materials Studio. This initial model was then geometry-optimized using the DMOL³ package.

Geometry optimizations were performed for each of the individual configurations that were generated with and without heteroatoms. Important demarcation arises from the position
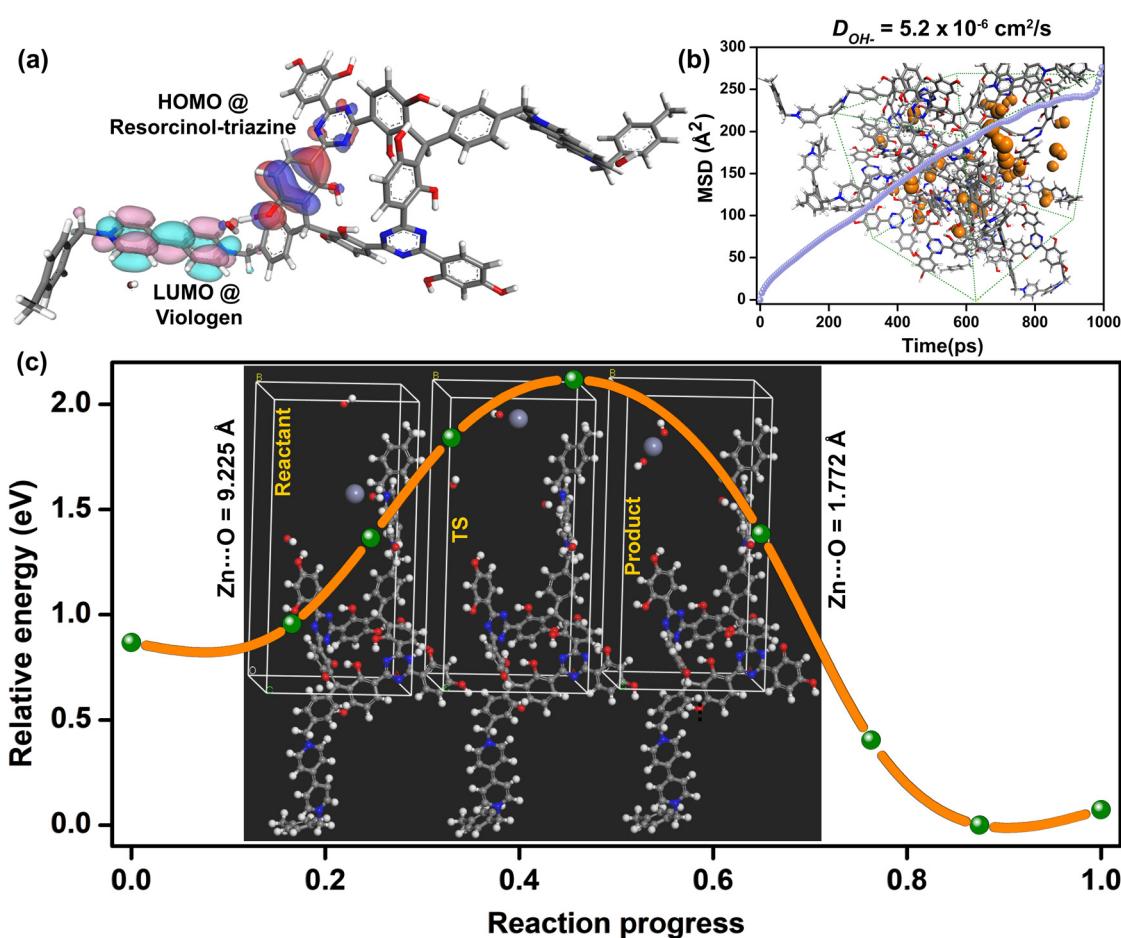
Fig. 5 Computational modeling: (a) Frontier orbital locations within the polymer backbone. The resorcinol-triazine can set up a push−pull with the e⁻ deficient viologen units. (b) Mean square displacement (MSD) *vs.* time plot calculated using MD simulations and the derived hydroxide ion self-diffusion coefficient. Inset shows a snapshot of an optimized structure with hydroxide ions shown as space fills. (c) Representative minimum energy path (MEP) for Zn²⁺ ion movement within the hydroxyl-containing polymer assessed from NEB.

of the HOMO and the LUMO. The **1_OH** compounds with conjugated triazine-resorcinol core covalently linked to the viologen units have the HOMO residing on the resorcinol ring and the triazine nitrogen, and to some extent on the hydroxyl groups that are located proximal to the viologen (Fig. 5a). Meanwhile, the LUMO resides mostly on the viologen rings. For the as-made polymer, the HOMO–LUMO gap turned out to be 0.03 eV. However, when the triazine rings are replaced with phenyl moieties, the all-carbon backbone does not demarcate much between the HOMO–LUMO levels, leading to a gap of 0.002 eV.

This removes the push–pull characteristics within the framework backbone. This points at how crucial the triazine nitrogens are in setting up the push–pull characteristics between the triazine-resorcinol unit and the viologen rings. Remarkably, this is only for the small section of the polymer. As the polymer grows into an amorphous extended cross-linked structure, there is bound to be a breakdown of the long-range conjugation assisted electronic transport. The overall bandgap will be much larger, and typically in the semiconducting regime.[31] However, the redox active localized regions are sufficient to set-up a push–pull effect, which would govern the movement of the hydroxide ions.

Diffusion coefficient of hydroxide ions in the viologen polymer

We resorted to MD simulations for garnering insights into the transport of hydroxide ions within the polymer framework. All structural dynamics were carried out using the Forcite module in the Materials Studio. An amorphous cell was constructed for a structure encompassing cross-linked chains. These were filled with hydroxide ions in an 8:32 ratio per unit cell. A rigorous geometry optimization was performed until excellent convergence was achieved. The optimized structure was further equilibrated using an NPT ensemble, and the average lattice parameters were employed to the output structure. The migration of the hydroxide ions in the cationic framework was explored under the NVT conditions. The final trajectory was obtained from a 1 ns microcanonical NVE dynamics with a large 50 Å cut-off distance performed at 300 K. The Mean Square Displacement (MSD) *vs.* time plots were used to calculate the average diffusion coefficient for the hydroxide ions, which turned out to be 5.2×10^{-6} cm^2 s^{-1} (Fig. 5b). However, the computed diffusion coefficient is lower than the experimental one (2.9×10^{-5} cm^2 s^{-1}). This is because the hydration was not considered in the MD simulations.[51] Importantly, the observed and calculated diffusion coefficients for the hydroxide ions were comparable with those available from the recent computational works.[52–55] From the fits to the MSD plots, we estimated the activation energy for the diffusion of the hydroxide ions in the cationic polymer framework to be 0.22 eV (21 kJ mol^{-1}, Fig. S27, ESI†), which is comparable to the experimental activation energy (0.153 eV) (14.77 kJ mol^{-1}) calculated using the Warburg Bode plot (Fig. S27, ESI†).[56]

Large energy barrier for zinc-ion incorporation into the cationic polymer

To estimate the energy barriers associated with the process of incorporation of the Zn^{2+} ions into the polymer and its interaction with the OH$^-$ ion, we used the Nudged Elastic Band calculations. In the "reactant" model, the Zn^{2+} ions were positioned relatively farther from the hydroxide ions present within the polymer's unit cell. Meanwhile, we configured the "product" to have the Zn^{2+} ions at a bonding distance to the hydroxide ions (Fig. 5c). The framework atoms of the "reactant" and "product" were made indistinguishable to sequester only the effect of Zn-ion incorporation. Then, a transition state confirmation for the bound state was performed using the climbing-image NEB method. We included multiple intermediate configurations between reactant–TS and TS–product to obtain a good extrapolation of the minimum energy path (MEP) and optimized under the NEB. The Ea for the Zn^{2+} ions incorporation was calculated using as much as 7 intermediate configurations.

Most importantly, both the reactants and the product configurations showed stable structures. Furthermore, the incorporation of the Zn^{2+} ions goes through an acceptable intermediate, but with a significant energy barrier (2.11 eV). We observe that the energy barriers for incorporating the zincate ion into the polymer were even higher, and the zincate species goes through some unacceptable geometry deformations due to repulsive interactions with the polymer's framework atoms. This reveals the non-compatibility of the Zn^{2+} ions and zincates in the polymer, which is a desirable feature in preventing zinc-dendrimer formation or cell short-circuiting.

Conclusions

This work describes a cationic polymer with counterbalancing hydroxide anions as a solid-state electrolyte for a zinc–air battery. The uniqueness of the work is its simplicity, despite delivering high performance. We couple Bakelite and viologen chemistry to make this polymer, which is exceptionally stable, easy to make, and affordable. The organic nature of this ion-conducting polymer (1.4×10^{-2} S cm^{-1} at 80 °C and 95% RH) enables it to integrate well with filter paper to yield an electrolyte requiring minimal KOH wetting. **1_OH@FP** delivers excellent performance as the separator-cum-electrolyte for the zinc–air battery with a power density of 115 mW cm^{-2}, which is three times more than the neat filter paper-based counterpart. The fabricated device easily withstands bending and twisting operations. A gradual and constant increment in OCV was observed for devices upon connecting them in series, enabling them to light up a power-demanding traffic signal for a long time. Computational modeling reveals the importance of heteroatoms in providing an electronic push–pull across the framework, which aids in transporting the hydroxide ions. At the same time, the MD simulations confirm the favorable diffusion of hydroxide ions and the high barrier for the undesirable penetration of Zn^{2+} ions into the polymer. Thus, our findings assert the readily accessible C–C-linked cationic polymer's capacity as solid-state electrolytes for ZAB and any anion conducting membrane.

Conflicts of interest

There are no conflicts to declare.

Acknowledgements

References

1   J. R. Varcoe, P. Atanassov, D. R. Dekel, A. M. Herring, M. A. Hickner, P. A. Kohl, A. R. Kucernak, W. E. Mustain, K. Nijmeijer, K. Scott, T. Xu and L. Zhuang, *Energy Environ. Sci.*, 2014, **7**, 3135–3191.

2   N. Chen, H. H. Wang, S. P. Kim, H. M. Kim, W. H. Lee, C. Hu, J. Y. Bae, E. S. Sim, Y.-C. Chung, J.-H. Jang, S. J. Yoo, Y. Zhuang and Y. M. Lee, *Nat. Commun.*, 2021, **12**, 2367.

3   D. R. Dekel, *J. Power Sources*, 2018, **375**, 158–169.

4   S. Tao, H. Xu, Q. Xu, Y. Hijikata, Q. Jiang, S. Irle and D. Jiang, *J. Am. Chem. Soc.*, 2021, **143**, 8970–8975.

5   K.-D. Kreuer, *Chem. Mater.*, 1996, **8**, 610–641.

6   Y. Meng, J. Gao, Z. Zhao, J. Amoroso, J. Tong and K. S. Brinkman, *J. Mater. Sci.*, 2019, **54**, 9291–9312.

7   L. Malavasi, C. A. J. Fisher and M. S. Islam, *Chem. Soc. Rev.*, 2010, **39**, 4370–4387.

8   S. S. Shinde, C.-H. Lee, A. Sami, D.-H. Kim, S.-U. Lee and J.-H. Lee, *ACS Nano*, 2017, **11**, 347–357.

9   Z. Li, W. Niu, Z. Yang, N. Zaman, W. Samarakoon, M. Wang, A. Kara, M. Lucero, M. V. Vyas, H. Cao, H. Zhou, G. E. Sterbinsky, Z. Feng, Y. Du and Y. Yang, *Energy Environ. Sci.*, 2020, **13**, 884–895.

10 S. Haldar, D. Kaleeswaran, D. Rase, K. Roy, S. Ogale and R. Vaidhyanathan, *Nanoscale Horiz.*, 2020, **5**, 1264–1273.

11 R. Kushwaha, S. Haldar, P. Shekhar, A. Krishnan, J. Saha, P. Hui, C. P. Vinod, C. Subramaniam and R. Vaidhyanathan, *Adv. Energy Mater.*, 2021, **11**, 2003626.

12 J. Fu, R. Liang, G. Liu, A. Yu, Z. Bai, L. Yang and Z. Chen, *Adv. Mater.*, 2019, **31**, 1805230.

13 W. Sun, F. Wang, B. Zhang, M. Zhang, V. Küpers, X. Ji, C. Theile, P. Bieker, K. Xu and C. Wang, *Science*, 2021, **371**, 46–51.

14 Y. Li and H. Dai, *Chem. Soc. Rev.*, 2014, **43**, 5257–5275.

15 Q. Liu, Y. Wang, L. Dai and J. Yao, *Adv. Mater.*, 2016, **28**, 3000–3006.

16 M. Yu, Z. Wang, C. Hou, Z. Wang, C. Liang, C. Zhao, Y. Tong, X. Lu and S. Yang, *Adv. Mater.*, 2017, **29**, 1602868.

17 F. Cheng and J. Chen, *Chem. Soc. Rev.*, 2012, **41**, 2172–2192.

18 N. S. V. Narayanan, B. V. Ashokraj and S. Sampath, *J. Electrochem. Soc.*, 2009, **156**, A863.

19 A. R. Mainar, E. Iruin, L. C. Colmenares, A. Kvasha, I. De Meatza, M. Bengoechea, O. Leonet, I. Boyano, Z. Zhang and J. A. Blazquez, *J. Energy Storage*, 2018, **15**, 304–328.

20 P. Chen, K. Zhang, D. Tang, W. Liu, F. Meng, Q. Huang and J. Liu, *Front. Chem.*, 2020, **8**, 372.

21 H. Miao, B. Chen, S. Li, X. Wu, Q. Wang, C. Zhang, Z. Sun and H. Li, *J. Power Sources*, 2020, **450**, 227653.

22 J. Park, M. Park, G. Nam, J.-s Lee and J. Cho, *Adv. Mater.*, 2015, **27**, 1396–1401.

23 D. Chen and M. A. Hickner, *ACS Appl. Mater. Interfaces*, 2012, **4**, 5775–5781.

24 Y. A. Elabd, *Mol. Syst. Des. Eng.*, 2019, **4**, 519–530.

25 Z. Cao, H. Hu, M. Wu, K. Tang and T. Jiang, *J. Mater. Chem. A*, 2019, **7**, 17581–17593.

26 J. Fu, J. Zhang, X. Song, H. Zarrin, X. Tian, J. Qiao, L. Rasen, K. Li and Z. Chen, *Energy Environ. Sci.*, 2016, **9**, 663–670.

27 S. Nandi, V. M. Dhavale, S. Shalini, U. Werner-Zwanziger, H. Singh, S. Kurungot and R. Vaidhyanathan, *Adv. Mater. Interfaces*, 2015, **2**, 1500301.

28 R. Illathvalappil, V. M. Dhavale, S. N. Bhange and S. Kurungot, *Nanoscale*, 2017, **9**, 9009–9017.

29 M. T. Tsehaye, F. Alloin, C. Iojoiu, R. A. Tufa, D. Aili, P. Fischer and S. Velizarov, *J. Power Sources*, 2020, **475**, 228689.

30 D. J. Arnot, M. B. Lim, N. S. Bell, N. B. Schorr, R. C. Hill, A. Meyer, Y.-T. Cheng and T. N. Lambert, *Adv. Energy Mater.*, 2021, **11**, 2101594.

31 Y. Kim, M. Künzel, D. Steinle, X. Dong, G.-T. Kim, A. Varzi and S. Passerini, *Energy Environ. Sci.*, 2022, **15**, 2610–2618.

32 Y. Zeng, P. Gordiichuk, T. Ichihara, G. Zhang, E. Sandoz-Rosado, E. D. Wetzel, J. Tresback, J. Yang, D. Kozawa and Z. Yang, *Nature*, 2022, **602**, 91–95.

33 A. P. Katsoulidis and M. G. Kanatzidis, *Chem. Mater.*, 2011, **23**, 1818–1824.

34 R. Paul, S. C. Shit, T. Fovanna, D. Ferri, B. Srinivasa Rao, G. T. K. K. Gunasooriya, D. Q. Dao, Q. V. Le, I. Shown, M. P. Sherburne, Q. T. Trinh and J. Mondal, *ACS Appl. Mater. Interfaces*, 2020, **12**, 50550–50565.

35 R. Dawson, E. Stöckel, J. R. Holst, D. J. Adams and A. I. Cooper, *Energy Environ. Sci.*, 2011, **4**, 4239–4245.

36 B. Li, R. Gong, W. Wang, X. Huang, W. Zhang, H. Li, C. Hu and B. Tan, *Macromolecules*, 2011, **44**, 2410–2414.

37 S. Nandi, U. Werner-Zwanziger and R. Vaidhyanathan, *J. Mater. Chem. A*, 2015, **3**, 21116–21122.

38 D. Chakraborty, S. Nandi, R. Kushwaha, D. Kaleeswaran and R. Vaidhyanathan, *Mater. Res. Bull.*, 2021, **146**, 111614.

39 D. Crespy, M. Bozonnet and M. Meier, *Angew. Chem., Int. Ed.*, 2008, **47**, 3322–3328.

40 E. Breitmaier and W. Voelter, *Carbon-13 NMR spectroscopy*, VCH Publishers Inc, United States, 1987, **26**, 351.

41 S. Haldar, D. Rase, P. Shekhar, C. Jain, C. P. Vinod, E. Zhang, L. Shupletsov, S. Kaskel and R. Vaidhyanathan, *Adv. Energy Mater.*, 2022, **12**, 2200754.

42 L. Feng, X. Zhang, C. Wang, X. Li, Y. Zhao, X. Xie and Y. Lv, *Int. J. Hydrogen Energy*, 2016, **41**, 16135–16141.

43 G. A. Ludueña, T. D. Kühne and D. Sebastiani, *Chem. Mater.*, 2011, **23**, 1424–1429.

44 D. W. Kang, M. Kang, H. Yun, H. Park and C. S. Hong, *Adv. Funct. Mater.*, 2021, **31**, 2100083.

45 U. Tröltzsch and O. Kanoun, *Electrochim. Acta*, 2012, **75**, 347–356.

46 J. Chen, P. Li, N. Zhang and S. Tang, *J. Mater. Chem. A*, 2022, **10**, 7146–7154.

47 S. H. Lee and J. C. Rasaiah, *J. Chem. Phys.*, 2013, **139**, 124507.

48 R. Vedalakshmi, V. Saraswathy, H.-W. Song and N. Palaniswamy, *Corros. Sci.*, 2009, **51**, 1299–1307.

49 H. Zhang, B. Zhang, Y. Yang, D. Ye, R. Chen, Q. Liao and X. Zhu, *Chem. Commun.*, 2021, **57**, 1258–1261.

50 Z.-L. Wang, D. Xu, J.-J. Xu and X.-B. Zhang, *Chem. Soc. Rev.*, 2014, **43**, 7746–7786.

51 V. Dubey and S. Daschakraborty, *J. Phys. Chem. B*, 2022, **126**, 2430–2440.

52 J. Chen, P. Li, N. Zhang and S. Tang, *J. Mater. Chem. A*, 2022, **10**, 7146–7154.

53 P. Prakash, A. Shylendran, B. Fall, M. J. Zdilla, S. L. Wunder and A. Venkatnathan, *J. Phys. Chem. C*, 2022, **126**, 4744–4750.

54 T. Zelovich, L. Vogt-Maranto, C. Simari, I. Nicotera, M. A. Hickner, S. J. Paddison, C. Bae, D. R. Dekel and M. E. Tuckerman, *Chem. Mater.*, 2022, **34**, 2133–2145.

55 C. Chandana, H. D. Singh, L. S. Leo, P. Shekhar, D. Rase, D. Chakraborty, C. P. Vinod and R. Vaidhyanathan, *J. Mater. Chem. A*, 2022, **10**, 15647–15656.

56 P. Prakash, J. Aguirre, M. M. Van Vliet, P. R. Chinnam, D. A. Dikin, M. J. Zdilla, S. L. Wunder and A. Venkatnathan, *J. Mater. Chem. A*, 2018, **6**, 4394–4404.